Photonic band gap in thin wire metamaterials

Kai Meng Hock[*]

Department of Physics, The University of Liverpool, Liverpool, L69 7ZE, United Kingdom
and The Cockcroft Institute, Daresbury, Warrington, WA4 4AD, United Kingdom

We investigate the band structure of a class of photonic crystals made from only thin wires. Using a different method, we demonstrate that a complete photonic band gap is possible for such materials. Band gap materials normally consist of space filling dielectric or metal, whereas thin wires occupy a very small fraction of the volume. We show that this is related to the large increase in scattering at the Brillouin zone boundary. The method we developed brings together the calculation techniques in three different fields. The first is the calculation of scattering from periodic, tilted antennas, which we improve upon. The second is the standard technique for frequency selective surface design. The third is obtained directly from low energy electron diffraction theory. Good agreements with experiments for left handed materials, negative materials, and frequency selective surfaces are demonstrated.

I. INTRODUCTION

Photonic crystals are metamaterials in which the propagating properties of electromagnetic waves on a subwavelength scale can be manipulated by modifying the structure of a dielectric or metallic material periodically. For certain structures, it is possible to have a photonic band gap, a range of frequency in which the electromagnetic waves cannot propagate. This discovery has led to significant development in applications for photonic devices [1] and better understanding in the production of color by some living things [2]. More recently, numerous applications to accelerators have been studied [3]. In recent years, a large variety of metamaterials have been developed. One example is left handed material, which has a negative index of refraction [4]. The element is shaped in such a way that the current induced would flow along curved paths, resulting in magnetic permeability. At a certain frequency range, both permittivity and permeability may become negative, leading to a negative index of refraction. Other examples are photonic band gap materials, which inhibit the propagation of electromagnetic waves over a certain frequency range, known as the band gap [5]. These can be made up of dielectric or metallic elements. Incident waves are scattered from these elements and undergo multiple scattering among them. For suitable combinations of element designs and lattice structures, band gaps can result.

Most photonic band gap materials are made from either space filling dielectric to provide for sufficient wave scattering [6], or closely spaced metal pieces to produce strong capacitive effects [5]. Thin wires that are continuous through space have been shown to produce a cutoff frequency, explained in terms of plasmon resonance, below which no electromagnetic waves can propagate [7,8]. A complete photonic band gap that appears in between passbands has not been demonstrated for photonic crystals made from only thin wires. Such a material, if possible, would be interesting because the lightweight nature and design possibilities of the

thin wires would offer significant new potential for applications.

The main difficulty in producing a complete gap for thin wires is the generally weak scattering due to the extremely small volume fraction that they occupy. However, it is known that when the half wavelength of the propagating wave corresponds to the dimension of a piece of wire, there could be a large increase in scattering [9]. We suggest that in order to create a photonic band gap, the wire element must be designed in such a way that its resonance frequency coincides with the expected band gap. This would then produce the scattering where it matters most and hopefully, with a judicious choice of lattice symmetry, produce a complete gap.

In order to investigate this possibility, we require a method that can compute the band structures of thin wire photonic crystals quickly and reliably. At present, calculation methods tend to use a combination of electromagnetic simulation method and the transfer matrix method [10]. There are a variety of the former, but the ones more commonly used for left handed materials involve discretization of all space in the unit cell, which may be classified as finite-difference time-domain (FDTD) or finite element method (FEM) [11]. Although efficient and accurate, it can still be time consuming when the amount of structural detail in the element increases. In particular, this can happen for thin wires with large aspect ratios. There is another electromagnetic simulation method known as Method of Moment [12] which is suitable for metallic elements and discretizes only the element. In particular, when the element consists only of thin wires, the method can become quite simple and efficient. The resulting speed would be useful when mapping out the large number of points in the band structure.

Consider the scattering of electromagnetic wave by one layer of thin wire elements. There is already a technique for this which is originally used for the design of frequency selective surfaces (FSS) [13]. Next, consider assembling the layers to calculate the multiple reflections between them. It turns out that there is also a technique for doing this in low energy electron diffraction (LEED) theory for scalar waves [14]. After some modifications, we find that the two tech-

---
[*]k.m.hock@dl.ac.uk

niques can be merged and applied to transmission, reflection, and band structure calculations for electromagnetic waves. The approach of treating the material as layers is similar to the transfer matrix method [15] used to calculate photonic band structure.

A frequency selective surface (FSS) consists of an array of metallic elements arranged periodically over a two-dimensional (2D) plane [13,16]. The elements normally consist of thin, flat metallic patterns that lie in the array plane. One or more arrays of these elements may be embedded in a stratified dielectric medium. This has the property of allowing only an electromagnetic wave in a certain frequency range to pass through, and has important applications such as in radomes and in absorbers. Many methods have been developed for FSS design. In this paper, we consider elements that can be modeled as thin wires, and develop a fast design method using a combination of techniques. We use a version of the periodic moment method (PMM) in which the multiple scattering for each array is calculated using the vector potential and electric potential [17,18]. This is followed by the use of a version of a cascading method to calculate the arrays embedded in a stratified dielectric medium [14,19,20].

The calculation using vector and electric potential is originally developed for a planar array of antennas made of thin wires that are tilted out of plane [17]. Calculating the E field in terms of vector and electric potentials seems to give better convergence property for tilted elements. In [18], the method is modified to remove a few of the approximations used and shown to give good agreement with measurement metamaterials consisting of split ring resonators, in which the elements are tilted out of plane. The method appears not to have been applied to FSS for which elements lie in plane. We believe that the improved convergence property should also carry over to FSS calculation, and show in this paper that this can be achieved without sacrificing the level of accuracy. The use of vector and electric potential for the E field means that transmission and reflection at dielectric interface cannot be calculated directly using the Fresnel coefficients. Hence the multiple scattering for an array embedded in a stratified medium cannot be carried out using the "bounce mode organization" treatment of the type described in [14]. Fortunately, methods already exist that can overcome this problem.

The cascading method makes use of the multiple scattering results for individual arrays, and combines them into multiple layers quickly at much lower computation cost than the "bounce mode organization" method. A cascading method has been developed over 30 years ago to assemble layers of atoms for electron diffraction calculation [14]. It is applied about ten years ago to photonic band structure calculations and is also widely used now for left handed materials [10], where it is known as the transfer matrix method. At about the same time, the cascading method in a similar form began to be applied to the FSS design [16,20]. In all three versions, the method uses the terms from the plane wave expansion in the multiple scattering calculation of each array, and combines a small number of them appropriately with those of the next layer. In electron diffraction calculation, these terms are called electron beams, in the transfer matrix method they are just electromagnetic waves, and in FSS they are called Floquet harmonics. In all cases, they are

plane waves, and we show that the original form developed for electron diffraction can be easily applied with very few modifications.

II. FORMALISM

Here, we develop the moment method for thin wire metamaterials. In Sec. II A, we consider a 2D planar array of thin wire elements that are periodic and tilted out of plane. We develop the method for calculating the scattering of an electromagnetic plane wave incident on the array. In Sec. II B, we review the methods used to calculate scattering of microwave from frequency selective surfaces (FSS), and scattering of electrons from crystal surfaces. We explain how these three methods can be combined to calculate wave propagation through a three-dimensional (3D) thin wire metamaterial.

A. Vector-electric potential method for tilted elements

In this section, we consider a single layer of elements that can be modeled as thin wires. This would include a large class of left handed materials. These are often made from thin copper strips printed on circuit boards to form continuous wires and split ring resonators. It would also include a small class of photonic crystals made from wires [8]. We develop a method that is suitable for the calculation of transmission and reflection for such metamaterials. The method is essentially a modification on an existing method for calculating multiple scattering in an array of wire antennas [17], which we shall call the vector-electric potential method.

This is a moment method, which involves calculating the E field from the current in each wire segment. Two main approximations are made in [17]. One is the use of pulsed basis function for the current, i.e., the current is approximated to a constant value over the segment. Another is as follows. First, the E-field calculation is decomposed into two terms, a vector potential term and an electric potential term. The electric potential term is calculated from the charge density on the segment. For a pulsed basis function, the charge density consists of two point charges at the ends of the segment, because the current terminates abruptly there. Each of these is approximated in [17] as a line charge centered at the corresponding point, and of the same length as the original segment. In fact, it is possible to carry out the calculation using the point charges. However, when the array plane of the observation point where the E field is calculated passes through a point charge, the plane wave sum diverges. (Plane wave sums for the vector and electric potentials are given in [17]. Plane wave sums for E fields are given in Sec. II B). Although, it is possible to try and select observation points such that their array planes do not pass through any segment end, this quickly becomes very difficult and inconvenient for a wire element that is not straight and has more than a few elements. This may be a reason for the use of the line charge approximation in [17].

Here, we make two modifications. Following Ref. [12], we replace the pulsed basis function with a sinusoidal basis function as follows:

$$I_j = A_j + B_j \sin \beta(s - s_j) + C_j \cos \beta(s - s_j). \qquad (1)$$

Suppose the wire element is divided into N_s segments. We approximate the current in the jth segment using the basis functions in Eq. (1). A_j, B_j, and C_j are the unknown coefficients, β is the magnitude of the wave vector, s is the distance along the wire, starting from 0 at the beginning of first segment, and s_j is the value of s at the center of the jth segment. The current is required to be continuous over the whole wire element. Apart from being more physical and having better convergence property, the smoothness also means that the point charges at the common ends of adjacent segments cancel exactly. The calculation of the E field can then be carried out for the given basis functions without the need to consider the point charges. We have thus removed the need to approximate these as line charges. In an earlier paper [18] where this method has been very briefly sketched out, we have shown that it is able to give good agreement with measurement on split ring resonators. Here, we show that it is also useful for left handed materials.

There are many variations on the method of moment. We use the following version for thin wires. Consider a simple wire element of finite length and zero radius. More complicated cases may be treated using techniques in [12]. The wire is first divided into segments. The current in each segment is approximated by a basis function multiplied by an unknown coefficient to be determined. The E field on the surface at the center of another segment due to this basis function is computed. The first segment is called the source segment, and the point on the second segment is called the observation point. The actual E-field contribution from the source segment is obtained by multiplying with the unknown coefficient. The total E field is obtained by adding together contributions from all segments of the wire, and then adding to the incident E field at the observation point. The component of this sum along the observation segment is set to zero for a perfect conductor, or related to the current at that segment using Ohm's law. Each observation point results in one equation with a number of unknown coefficients. The resulting linear system of equations can then be solved. The coefficients obtained are then used to calculate the actual current in each segment and, from this, the scattered field. We use the point matching method, in which only values of the incident E field at the observation points are required. The formulas developed are given in Appendix A.

B. Direct E-field method for planar elements

The results in Sec. II A can be used to calculate scattering from multiple arrays by using a cascading method, which will be described in Sec. II C. Here, we list a set of formulas that are widely used in the engineering literature to calculate scattering from a single layer of planar elements, usually in the form of frequency selective surfaces. These can only be used for elements that are not tilted out of plane. We list them here because they are very well established in the engineering literature, and will serve as a useful comparison in Sec. II C with the method described in Sec. II A, which have not previously been published.

We list the expressions required for direct E-field calculation [13], using the sinusoidal basis function of the same type as in Eq. (1) in order to facilitate comparison. In the thin wire approximation, the wire element is divided into N_s segments. From the results in [12,21], the E field due to this current at any point $\mathbf{R}$ can be written in the following form:

$$\mathbf{E}(\mathbf{R}, \mathbf{R}_j) = A_j \mathbf{E}_0(\mathbf{R}, \mathbf{R}_j) + B_j \mathbf{E}_s(\mathbf{R}, \mathbf{R}_j) + C_j \mathbf{E}_c(\mathbf{R}, \mathbf{R}_j), \quad (2)$$

where $\mathbf{E}_0$ is the E field when I_j is 1, $\mathbf{E}_s$ is the E field when I_j is $\sin \beta(s - s_j)$, and $\mathbf{E}_c$ is when I_j is $\cos \beta(s - s_j)$. These are in turn given by the following plane wave sums:

$$\mathbf{E}_0 = \frac{Z}{2D_x D_z} \sum_{k=-\infty}^{\infty} \sum_{n=-\infty}^{\infty} \frac{\exp[-j\beta(\mathbf{R}_i - \mathbf{R}_j) \cdot \hat{\mathbf{r}}_\pm]}{r_y}$$
$$\times \mathrm{sinc}(\beta \hat{\mathbf{p}}_j \cdot \hat{\mathbf{r}}_\pm l_j/2) \overline{\mathbf{e}}_\pm, \qquad (3)$$

$$\mathbf{E}_c = \frac{\mathbf{E}_{+1} + \mathbf{E}_{-1}}{2}, \qquad (4)$$

and

$$\mathbf{E}_s = \frac{\mathbf{E}_{+1} - \mathbf{E}_{-1}}{2j}, \qquad (5)$$

where

$$\mathbf{E}_{+1} = \frac{Z}{2D_x D_z} \sum_{k=-\infty}^{\infty} \sum_{n=-\infty}^{\infty} \frac{\exp[-j\beta(\mathbf{R}_i - \mathbf{R}_j) \cdot \hat{\mathbf{r}}_\pm]}{r_y}$$
$$\times \mathrm{sinc}[(1 + \beta \hat{\mathbf{p}}_j \cdot \hat{\mathbf{r}}_\pm) l_j/2] \overline{\mathbf{e}}_\pm, \qquad (6)$$

$$\mathbf{E}_{-1} = \frac{Z}{2D_x D_z} \sum_{k=-\infty}^{\infty} \sum_{n=-\infty}^{\infty} \frac{\exp[-j\beta(\mathbf{R}_i - \mathbf{R}_j) \cdot \hat{\mathbf{r}}_\pm]}{r_y}$$
$$\times \mathrm{sinc}[(-1 + \beta \hat{\mathbf{p}}_j \cdot \hat{\mathbf{r}}_\pm) l_j/2] \overline{\mathbf{e}}_\pm, \qquad (7)$$

and $\overline{\mathbf{e}}_\pm = [\hat{\mathbf{p}}_j \times \hat{\mathbf{r}}_\pm] \times \hat{\mathbf{r}}_\pm$. $\hat{\mathbf{p}}_j$ is a unit vector parallel to segment j, and l_j the length of the segment. $\hat{\mathbf{r}}_\pm$ is given in Appendix A. Equations (4) and (5) are based on the relation between $\sin x$, $\cos x$, and $\exp(\pm jx)$. Equation (3) is explained in [13]. Equations (6) and (7) are derived in a similar way for I_j equal to $\exp(jx)$ and $\exp(-jx)$, respectively. These equations can be used to calculate scattering from elements that lie in the array plane, but not when they are tilted out of plane. The close relationship with the method in Sec. II A, which can be used for tilted elements, is explained in Appendix B.

As in Sec. II A, the unknown coefficients are obtained by relating these to the incident E field and the wire resistance. Ohm's law gives

$$\sum_{j=1}^{N_s} V_{ij} = \overline{I}_i \overline{Z}_i, \qquad (8)$$

where $\overline{Z}_i$ is the impedance of segment i, which we approximate using the impedance per unit length of an infinitely long cylinder [22]. The total voltage on segment i is approximated by

$$V_{ij} = (\mathbf{E}_i^{\text{inc}} + \mathbf{E}_{ij}) \cdot \mathbf{p}_i l_i, \tag{9}$$

where $\mathbf{E}_{ij} = \mathbf{E}(\mathbf{R}_i, \mathbf{R}_j)$. The incident field $\mathbf{E}_i^{\text{inc}}$ will be obtained later from one of the plane wave terms used in the cascading method.

C. Cascading method for multiple layers

We list here the expressions for the cascading method use in electron diffraction theory. These have been explained in [14]. The relation between the plane wave amplitudes on the one side of layer m, and those on the other side is given by

$$
\begin{aligned}
a_{m\mathbf{g}'}^+ = \sum_{\mathbf{g}} &\left[I_{\mathbf{g}'\mathbf{g}} + M_{\mathbf{g}'\mathbf{g}}^{++}(m) \right] \\
&\times \exp\left[-i\left(\mathbf{K}_{\mathbf{g}}^+ \cdot \frac{1}{2}\mathbf{c}_{m-1} + \mathbf{K}_{\mathbf{g}'}^+ \cdot \frac{1}{2}\mathbf{c}_m \right) \right] a_{m-1\mathbf{g}}^+ + M_{\mathbf{g}'\mathbf{g}}^{+-}(m) \\
&\times \exp\left[-i\left(-\mathbf{K}_{\mathbf{g}}^- \cdot \frac{1}{2}\mathbf{c}_m + \mathbf{K}_{\mathbf{g}'}^+ \cdot \frac{1}{2}\mathbf{c}_m \right) \right] a_{m\mathbf{g}}^- \\
= \sum_{g} &Q_{\mathbf{g}'\mathbf{g}}^{\text{I}}(m) a_{m-1\mathbf{g}}^+ + Q_{\mathbf{g}'\mathbf{g}}^{\text{II}}(m) a_{m\mathbf{g}}^-, \tag{10}
\end{aligned}
$$

and

$$
\begin{aligned}
a_{m-1\mathbf{g}'}^- = \sum_{\mathbf{g}} &\left[I_{\mathbf{g}'\mathbf{g}} + M_{\mathbf{g}'\mathbf{g}}^{--}(m) \right] \\
&\times \exp\left[-i\left(-\mathbf{K}_{\mathbf{g}}^- \cdot \frac{1}{2}\mathbf{c}_m - \mathbf{K}_{\mathbf{g}'}^- \cdot \frac{1}{2}\mathbf{c}_{m-1} \right) \right] a_{m\mathbf{g}}^- \\
&+ M_{\mathbf{g}'\mathbf{g}}^{-+}(m)\exp\left[-i\left(-\mathbf{K}_{\mathbf{g}'}^- \cdot \frac{1}{2}\mathbf{c}_{m-1} \right.\right. \\
&\left.\left. + \mathbf{K}_{\mathbf{g}}^+ \cdot \frac{1}{2}\mathbf{c}_{m-1} \right) \right] a_{m-1\mathbf{g}}^+ = \sum_{g} Q_{\mathbf{g}'\mathbf{g}}^{\text{IV}}(m) a_{m\mathbf{g}}^- \\
&+ Q_{\mathbf{g}'\mathbf{g}}^{\text{III}}(m) a_{m-1\mathbf{g}}^+. \tag{11}
\end{aligned}
$$

Note that we follow the convention in engineering and have reversed the signs of the wave vectors in the exponentials, since many of the formulas in this paper originated from the engineering literature. The link between this and the FSS equations above becomes clear once we identify the following relation between the wave vectors:

$$\mathbf{K}_{\mathbf{g}}^{\pm} = \beta \hat{\mathbf{r}}_{\pm}. \tag{12}$$

$M_{\mathbf{g}'\mathbf{g}}^{+-}$, for example, is the amplitude scattered into $\hat{\mathbf{r}}_+'$ from the wave incident along $\hat{\mathbf{r}}_-$. Note that in electron diffraction, it is sufficient to treat the electrons as scalar waves. Since electromagnetic waves have two polarizations, $M_{\mathbf{g}'\mathbf{g}}^{+-}$ would therefore be expanded into a 2×2 matrix. Defining the following two polarization directions,

$$\mathbf{n}_{\perp} = \frac{\hat{\mathbf{r}} \times \mathbf{n}_D}{|\hat{\mathbf{r}} \times \mathbf{n}_D|} \quad \text{and} \quad \mathbf{n}_{\parallel} = \hat{\mathbf{r}} \times \mathbf{n}_{\perp}, \tag{13}$$

where $\mathbf{n}_D$ is a unit vector normal to the layer, the 2×2 matrix would contain the amplitudes scattered into polarization $\mathbf{n}_{\perp}$ or $\mathbf{n}_{\parallel}$, from the wave incident with polarization $\mathbf{n}_{\perp}$ or $\mathbf{n}_{\parallel}$. $a_{m\mathbf{g}}^{\pm}$ are likewise expanded into a 2×1 column vector con-

taining the amplitudes for the $\mathbf{n}_{\perp}$ and $\mathbf{n}_{\parallel}$ polarizations. The layers can then be assembled in pairs by the following expressions:

$$Q^{\text{I}}(12) = Q^{\text{I}}(2)[I - Q^{\text{II}}(1)Q^{\text{III}}(2)]^{-1}Q^{\text{I}}(1),$$

$$Q^{\text{II}}(12) = Q^{\text{II}}(2) + Q^{\text{I}}(2)Q^{\text{II}}(1)[I - Q^{\text{III}}(2)Q^{\text{II}}(1)]^{-1}Q^{\text{IV}}(2),$$

$$Q^{\text{III}}(12) = Q^{\text{III}}(1) + Q^{\text{IV}}(1)Q^{\text{III}}(2)[I - Q^{\text{II}}(1)Q^{\text{III}}(2)]^{-1}Q^{\text{I}}(1),$$

$$Q^{\text{IV}}(12) = Q^{\text{IV}}(1)[I - Q^{\text{III}}(2)Q^{\text{II}}(1)]^{-1}Q^{\text{IV}}(2). \tag{14}$$

The Q matrices are as defined in Eqs. (10) and (11). Note that Q^{I}, Q^{IV} are for transmission, and Q^{II}, Q^{III} are for reflection. We do not make any claim about the use of these expressions for FSS except that they are convenient.

An important practical aspect of FSS is the stratified dielectric medium in which the array or arrays have to be embedded for applications. This can be treated by constructing the Q matrices for each and every dielectric interface and layer. The Q matrices for an interface are constructed from the following Fresnel coefficients, defined in [13]. Following the notations there, we have, for reflection between layers 1 and 2,

$$^E_{\perp}\Gamma_{1,2} = \frac{Z_2 r_{1y} - Z_1 r_{2y}}{Z_2 r_{1y} + Z_1 r_{2y}}, \quad ^E_{\parallel}\Gamma_{1,2} = \frac{Z_2 r_{2y} - Z_1 r_{1y}}{Z_2 r_{2y} + Z_1 r_{1y}}, \tag{15}$$

and for transmission,

$$^E_{\perp}T_{1,2} = 1 + {}^E_{\perp}\Gamma_{1,2}, \quad ^E_{\parallel}\Gamma_{1,2} = 1 + {}^E_{\parallel}\Gamma_{1,2}. \tag{16}$$

Then $Q_{\mathbf{g}'\mathbf{g}}^{\text{I}}$ and $Q_{\mathbf{g}'\mathbf{g}}^{\text{III}}$ are null 2×2 matrices since the interface has no periodicity, unless $\mathbf{g}' = \mathbf{g}$, when

$$Q_{\mathbf{g}\mathbf{g}}^{\text{III}} = \begin{pmatrix} {}^E_{\perp}\Gamma_{1,2} & 0 \\ 0 & -{}^E_{\parallel}\Gamma_{1,2} \end{pmatrix}, \tag{17}$$

and

$$Q_{\mathbf{g}\mathbf{g}}^{\text{I}} = \begin{pmatrix} {}^E_{\perp}T_{1,2} & 0 \\ 0 & {}^E_{\parallel}T_{1,2}\dfrac{r_{1y}}{r_{2y}} \end{pmatrix}. \tag{18}$$

Likewise for $Q_{\mathbf{g}'\mathbf{g}}^{\text{IV}}$ and $Q_{\mathbf{g}'\mathbf{g}}^{\text{II}}$ but with indices 1 and 2 interchanged. Notice the factor of r_{1y}/r_{2y} for $_{\parallel}\Gamma$ required by the convention in [13]. More importantly, note that an additional negative sign is required for $_{\parallel}\Gamma$ because $\mathbf{n}_{\parallel}$ is reflected in the incidence normal on reflection.

The Q matrices between two adjacent interfaces are constructed as follows. Within the same dielectric layer, no reflection is involved, so $Q_{\mathbf{g}'\mathbf{g}}^{\text{II}}$ and $Q_{\mathbf{g}'\mathbf{g}}^{\text{III}}$ are all zero 2×2 matrices. $Q_{\mathbf{g}'\mathbf{g}}^{\text{I}}$ and $Q_{\mathbf{g}'\mathbf{g}}^{\text{IV}}$ simply have to provide the necessary phase factors for transmission through the layer thickness. So they are zero 2×2 matrices unless $\mathbf{g}' = \mathbf{g}$, when

$$Q_{\mathbf{g}'\mathbf{g}}^{\text{I}} = \begin{pmatrix} \exp(-j\beta d_m \mathbf{n}_D \cdot \mathbf{r}_+ n_r) & 0 \\ 0 & \exp(-j\beta d_m \mathbf{n}_D \cdot \mathbf{r}_+ n_r) \end{pmatrix}, \tag{19}$$

and

$$Q_{\mathbf{g}'\mathbf{g}}^{\mathrm{IV}} = \begin{pmatrix} \exp(-j\beta d_m \mathbf{n}_D \cdot \mathbf{r}\_n_r) & 0 \\ 0 & \exp(-j\beta d_m \mathbf{n}_D \cdot \mathbf{r}\_n_r) \end{pmatrix},$$

(20)

where d_m is the thickness of the mth dielectric layer, and n_r is the refractive index.

In order to obtain the band structure, the Bloch waves are first computed by [14]

$$\begin{bmatrix} Q^{\mathrm{I}} & Q^{\mathrm{II}} \\ -[Q^{\mathrm{IV}}]^{-1} Q^{\mathrm{III}} Q^{\mathrm{I}} & [Q^{\mathrm{IV}}]^{-1}[I - Q^{\mathrm{III}} Q^{\mathrm{II}}] \end{bmatrix} \begin{bmatrix} b_{i-1}^+ \\ b_i^- \end{bmatrix}$$

$$= \exp(-i\mathbf{k} \cdot \mathbf{c}) \begin{bmatrix} b_{i-1}^+ \\ b_i^- \end{bmatrix}$$

(21)

for each frequency and $\mathbf{K}_\parallel$. In principle, the corresponding k_y can then be obtained from the eigenvalues when these are equal to 1. Except for the reversal in sign of $\mathbf{k}$, both the above sets of equations can be used directly without further modification.

There are a few convergence issues in this method. One is the tolerance of the sum of the plane wave expansion in the FSS calculation. Another is the number of segments needed to model each wire element. A third is the number of beams required for the Q-matrices calculation. In the following calculations, we have found that a tolerance smaller than 0.001 does not make much difference to the final results. The plane wave sum in one layer is the most time consuming part of the calculation, and depends directly on the number of segments N_s. We try to minimize this, so the convergence has to be checked by varying N_s. We define N_g to be the number such that every beam (n,k) for which $\sqrt{n^2+k^2}$ does not exceed this value is included. We found that in all cases below, convergence is achieved for $N_g=2$. Calculation of the Q matrices is much faster than the plane wave sum, as is the final assembly of the layers.

III. RESULTS AND DISCUSSION

In Sec. III A, we apply the vector-electric potential method to a left handed material (LHM) for which experimental result is available. The LHM is fabricated from flat, printed strips that are very close together at some positions, and therefore deviate significantly from the thin cylindrical wire radius assumed in the method developed. Nevertheless, some agreement is obtained and the discrepancies serve as a useful illustration on the range of validity of the method. In Sec. III B, we apply all three methods to a number of frequency selective surfaces (FSS). These are also fabricated from printed strips, but the strips here are much narrower and further apart from one another. The condition is therefore much closer to the thin wire assumption in the method, and excellent agreement with measurement is obtained. In Sec. III C, we first apply the methods to a negative material for comparison with experiment. We also repeat the calculation for the LHM in Sec. III A, treating it as three separate layers instead of a single layer. We then design a 3D metamaterial from thin wires alone, and demonstrate by calculation that a complete photonic band gap can exist.
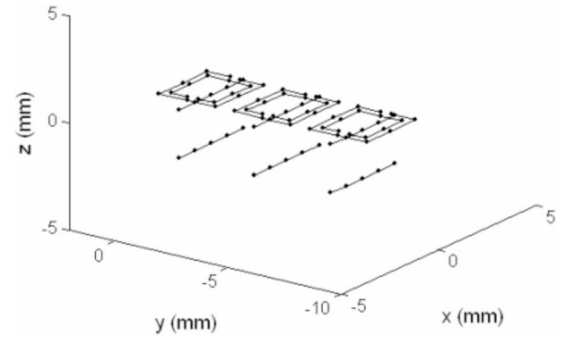

FIG. 1. Thin wire model of the left handed material in [4]. The dots represent the junctions of the segments used.

A. Left handed material

It has already been shown in [18] that this method can give good agreement with experiments for split ring resonators. In this section, we present a comparison with a more complex structure—that of a three layer, left handed material. We model the printed circuit structure of split rings and continuous wires in [4] using thin wires. Our model is shown in Fig. 1. Two approximations have to be made. The printed circuit creates the rings and wires from flat copper strips. These are approximated by thin cylindrical wires. In doing so, we need to decide what cylindrical radius to use. Reference [9], based on considerations on capacitance of the infinitely on strip, suggests a quarter of the width of the printed strip. In a unit cell in Fig. 1, this would lead to a distance of only one diameter between the split rings and one of the continuous wires, which is too close according to [12], and produces transmission amplitudes exceeding 1 at the passband near 14 GHz (crosses in Fig. 2). Instead, we choose one-twelfth of the strip width, a value that just brings down the amplitudes below 1 (dots in Fig. 2). The significance of this will be discussed later. Next, the method requires a homogeneous medium. The substrate of the printed circuit is perpendicular to the array plane and of different permittivity to the Rohacell foam spacer in between. We have to approximate it to a continuous medium. We took the volume average of 1.12, and hope that it is reasonable because the substrate is much thinner than the spacer.

The results of the calculated R and T are shown in Fig. 2 by the dotted curves. We have repeated the calculation using double the number of segments in Fig. 1 and obtained nearly the same results. To check for convergence of the plane wave sums for the vector and electric potentials, we set a tolerance value such that if the sum changes by a fraction that is less than the tolerance when N_g is increased by 1, we accept that the sum has converged. The results in Fig. 2 are obtained using a tolerance of 0.001. We find that reducing the tolerance to 0.0001 produces almost the same results. The agreement with measurement is fairly good, and the passband is reproduced correctly near 14 GHz. Discrepancies may be attributed to the approximations described above. In order to understand the discrepancies, we consider the three main areas in which the calculation conditions deviate from measurement conditions. These are the approximation to a homogeneous medium, the assumption of zero end cap currents,
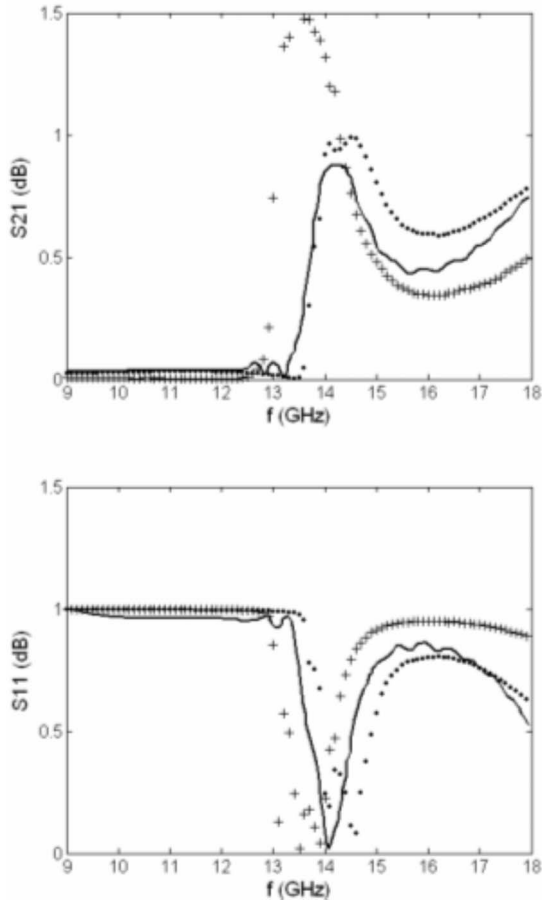
FIG. 2. The solid curves are the measured results of the left handed material in [4]. The crosses are calculated using an equivalent radius of a quarter of the copper strip width, and the dots are calculated using one-twelfth of the strip width.

and the modeling of a flat strip with a cylindrical wire. The approximation of the current using sinusoidal basis functions has already been validated by checking that the results converge when the segment number is increased.

The substrate material supporting the copper strips has a dielectric constant of 2.2 and thickness of 0.025 cm. The two substrate films present in each unit cell would cause scattering that can modify the actual E field arriving at each segment. A simple calculation of a normally incident plane wave on such a film gives a transmission of the order of -0.01 dB. This corresponds to an attenuation of about 0.001. Since the strongest E-field contribution comes from segments in the same and adjacent unit cells, we may expect the extra scattering to be dominated by a small number of substrate films. To obtain an upper estimate of the effect, we introduce a random error that is ten times larger—an error of 0.01 on each of the computed E fields. The resulting R and T differ by at most 1%, which is much smaller than the observed discrepancies in Fig. 2.

Next, we consider the end cap current. This is the current flowing into the finite area at the tip of each wire end, so that the length of the wire is effectively increased. It is known [22] that at resonance, the length of a wire is related to the half wavelength. Since the passband in Fig. 2 can be attrib-

uted to negative permeability arising from resonance in the split ring resonators, we may expect that it would shift slightly if the end cap current is taken into account. As an upper estimate, we introduce an extra length of one-quarter the strip width to each of the four ends of the split ring resonators for each unit cell in Fig. 1. The resulting R and T are indeed shifted to lower frequency by about 1%, which is close to the fractional increase in the length of each split ring resonator. This is also insufficient to explain the discrepancies.

Finally, we consider the effect of modeling a flat strip with a cylindrical wire. (Note that the strip is 250 μm wide and 17 μm thick. The thickness is not given in Ref. [4]. The value stated here is obtained from Ref. [23], published by nearly the same group of authors.) This can be studied qualitatively by varying the equivalent radius of the wire. When the radius is one-quarter the strip width, the surface area is closer to that of the strip, but the shape is very different. When it is one-twelfth the strip width, the diameter is closer to the strip thickness, but the surface area is very different. The results of calculation using these two equivalent radii are shown, respectively, in crosses and dots in Fig. 2. For the larger radius, the transmission near 14 GHz exceeds 1, for reasons explained above, and should be ignored as unphysical. Otherwise, the measured results fall in or close to the envelope formed by the dots and crosses over most of the frequency range. This strongly suggests that approximating the strip with a cylindrical wire is the main source of error. In Ref. [4], a 3D full wave electromagnetic simulation software is used to simulate the element and gives better agreement. This is because it can take into account the actual shapes of the printed strips by a finite element meshing.

On the other hand, this method has certain advantages of simplicity and efficiency, whether in meshing, coding, or computation. Despite discrepancies, the results in Fig. 2 show that it can provide reasonable estimates and correct features even when the elements are not made up of cylindrical wires. It is therefore useful for testing out new ideas on metamaterials, particularly when quick answers are needed for a variety of different designs.

B. Frequency selective surface

We apply the above combination of methods to a multilayer FSS illustrated by Fig. 4 of [24]. The measurement in [24] has been carried out by the author, and is used in Fig. 3 in this section for comparison with the calculation. This consists of four layers of straight wire arrays embedded in 1.7-mm-thick Kevlar. Each wire element is made by etching on a printed circuit, and is a copper strip of length 8 mm and width 80 μm, at some angle ψ to the x axis. Each array is a square lattice, with lattice constant 9 mm in both x and z directions. (The y direction in [24] corresponds to the z direction in this paper.) The four pieces of Kevlar are separated from one another by foam spacers. The full specification of the FSS is reproduced here in Table I. The measured permittivity of the Kevlar alone is 3.65, and that of the foam is 1.035. (These are different from [24], and are obtained from separate measurements by the author.) Each Kevlar layer
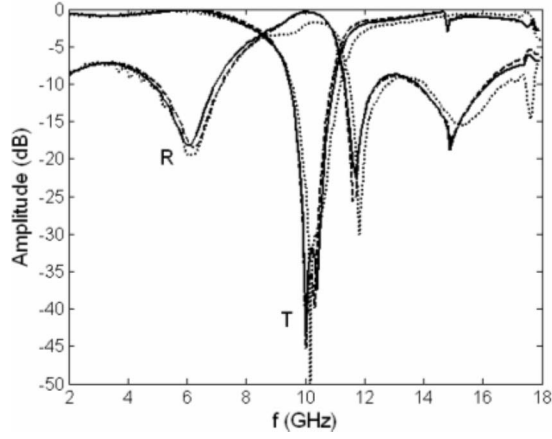
FIG. 3. T represents the transmitted amplitude, and R represents the reflected amplitude. The dotted curves are the measurement results from Fig. 5(b) in [24]. The solid curves are calculated from the vector or potential method, and the dashed curves are calculated from the direct E-field method.

tends to be slightly curved after fabrication, so when they are assembled with the foam spacers, there could be some air gap between Kevlar and foam. This could have led to the difference between calculation and measurement in [24]. Here, we show that by varying the foam thicknesses slightly, it is possible to obtain much better agreement with measurement.

We apply both the vector-electric potential method and the direct E-field method to calculate the Q matrices for the wire arrays in layers 1, 3, 5 and 7, for the original incident angle of 20° in the xy plane, with the E field parallel to the plane of incidence. The 15 sets of Q matrices are then constructed for the interfaces and arrays listed in Table II. Sets 3, 7, and 11 are identical and need only be computed once. Likewise for sets 5, 9, and 13. We find that when we use the nominal thicknesses of the foam spacers, we obtain results that are nearly the same as those calculated results shown in Fig. 5(b) of [24]. We then vary these and find that that the reflection peaks are quite sensitive to the spacer thicknesses. In contrast, the transmission peak hardly changes. We vary all of the foam thicknesses by the same amount each time, and find that a common increase of 1 mm in every spacer gives much better agreement, as shown in Fig. 3. Hence the reason for using the spacer thicknesses given above for Q matrices with set numbers 4, 8, and 12.

TABLE I. Specification of the multilayer FSS.

Layer	Description
1	Kevlar, $\psi=90°$
2	Foam, nominal thickness 1.0 mm
3	Kevlar, $\psi=45°$
4	Foam, nominal thickness 1.5 mm
5	Kevlar, $\psi=-45°$
6	Foam, nominal thickness 1.0 mm
7	Kevlar, $\psi=0°$

TABLE II. Interfaces and arrays in the FSS.

Set	Description
1	Interface from air to Kevlar
2	Wire array in layer 1
3	Interface from Kevlar to foam
4	Foam thickness of 2 mm
5	Interface from foam to Kevlar
6	Wire array in layer 2
7	Interface from Kevlar to foam
8	Foam thickness of 2.5 mm
9	Interface from foam to Kevlar
10	Wire array in layer 3
11	Interface from Kevlar to foam
12	Foam thickness of 2 mm
13	Interface from foam to Kevlar
14	Wire array in layer 4
15	Interface from Kevlar to air

Note the close agreement between the vector-electric potential method and the direct E field method. The former requires an additional approximation to calculate the potential gradient over a small distance δl, around the observation point of each segment. The agreement shows that this approximation is valid. It should be more accurate if δl is smaller, but if δl is too small, the result would become dominated by error due to the level of machine accuracy. For this case, we have chosen δl to be 1% of the segment length.

We have chosen $N_s=4$ for the wire element in each array. We have checked that the result is almost unchanged for $N_s=8$. We set a tolerance level for convergence of each plane wave sum to be 0.001, and checked that a tolerance of 0.0001 gives no noticeable difference to the calculation results in Fig. 3. For a tolerance of 0.001, we found that N_g is about 70 for convergence in the vector-electric potential method, and 700 for the direct E-field method. An increase of N_g by 10 times means an increase of 10^2 plane wave terms, resulting in the difference in computation times of up to two orders of magnitude between the two methods, as shown in Fig. 4.

For the cascading method, we apply Eq. (14) repeatedly to assemble the 15 sets of Q matrices listed above. Before doing so, we have to determine how many plane wave terms to include into each Q matrix. We find that convergence is achieved when $N_g=2$. This means nine plane wave terms, each with two polarizations, so that the size for each Q matrix is 18×18. Of course, this has to be confirmed by computing the result for $N_g=3$, when the size for each Q matrix is 50×50. This means that significant storage may be required for the cascading method, a tradeoff for the savings in computation time. We use a program written in MATLAB for the cascading, which takes 76 s to produce Fig. 3 from the computed Q matrices. It should be much faster if written in C and properly optimized. For $N_g=3$, we find that a set of four Q matrices stored in single precision, for a single array of wires requires 324 KB for each frequency point. Figure 3
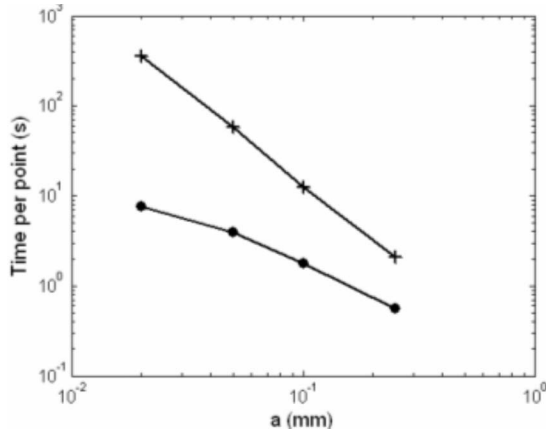
FIG. 4. The dots represent the computation time per frequency point for one array, for the vector-electric potential method. The crosses represent the time for the direct E-field method.

is computed at intervals of 0.1 GHz,and requires 50.3 MB for all the Q matrices of one array. We only store the Q matrices of set numbers 2, 6, 10, and 14 for the four arrays. The other Q matrices are generated on the fly as required. However, if necessary, the Q matrices for each array may also be generated on the fly from the calculated V_{ij} [in Eq. (9)] of that array. This took only 43 seconds for one array over the above frequency range on our 3 GHz computer, using CLAPACK. In contrast, the calculation of V_{ij} over the frequency range for the multiple scattering of one array takes 16 hours for the direct E-field method, and 20 minutes for the vector-electric potential method. The long computation time is due to the very small radius of 20 μm assumed for the equivalent wire radius. A larger radius that is still small compared with the wire length would give similar results, at much smaller computation time as shown in Fig. 4. Since we are modeling the flat copper strips as cylindrical wires, a larger radius may be chosen as an approximation if a quick estimate is required.

The calculated results agree well with the measured results. The discrepancies may be attributed to differences between the calculation and simulation conditions. One difference is that the spacing between arrays is likely to be nonuniform because the Kevlar samples are curved. Another is the finite size of the sample. A third is the presence of losses in the Kevlar and foam. Using the measurement method described in [24], it has not been possible to measure the imaginary part of the permittivity for these two materials as they are below noise level. However, sharp peaks (or nulls) in Fig. 3 are likely to be sensitive to losses even if they are small.

Figure 4 compares the computation time per frequency point for the two methods. This computation time is only the time for calculating the multiple scattering [V_{ij} in Eq. (9)] for one array. These are plotted against a, the wire radius. The wire radius strongly affects the computation time because it determines the height of the observation point above the array plane of the axis of a source segment. This height is the y coordinate of $\mathbf{R}_i - \mathbf{R}_j$ in Eqs. (3)–(7), and determines the exponentially decaying part of the sum because the y coordinate of $\hat{\mathbf{r}}_{\pm}$ is imaginary for large (k,n). Thus, as the wire

radius decreases, the observation point approaches the array plane of the source segment, and the exponential function decays more slowly, leading to slower convergence. The smallest a plotted in Fig. 4 is the equivalent radius of 20 μm that is used in the calculation of Fig. 3. This is taken as a one-quarter of the copper strip width on the array as suggested in Ref. [9]. The largest a is taken as 1/8 of the segment length we have used, which is 2 mm for the wire length of 8 mm and $N_s = 4$. According to [8], 1/8 the segment length is the largest radius that should be used for the thin wire approximation. Therefore, Fig. 4 gives an overview of the computation time required for a typical range of wire radii. The codes for the calculation, which have not been optimized, are written in C language, and are run on a 3 GHz computer.

There is one limitation for the cascading method. If the dielectric layers are very thin, a large number of plane wave terms may be required for convergence, and storage of the large Q matrices could become a problem. The reason is that the attenuation of a plane wave reaching the interface of the dielectric layer containing an array depends on (n,k), as determined by Eqs. (3)–(7). If convergence is achieved when $N_g = 2$, it means that plane wave terms with $\sqrt{n^2 + k^2}$ more than 2 have decayed enough to be neglected when they reach the interface. For a thinner layer, the interface would come closer to the array, and only plane wave terms with larger $\sqrt{n^2 + k^2}$ would have decayed sufficiently. Thus more plane waves have to be included in the cascading and a larger value of N_g would be required for convergence, hence larger Q matrices.

C. Photonic band gap

We begin by testing the method on a negative epsilon material. The construction and measurement results are given by Figs. 8 and 11 in Ref. [7]. As this involves wires that are continuous across adjacent unit cells, an additional condition has to be imposed on the current along the wire element. A wire segment at the unit cell boundary is joined to a segment in the adjacent cell. The condition is that the current along the latter segment differs from that along the corresponding segment in the original unit cell by a factor of $\exp(-i\mathbf{K}_{\parallel} \cdot \mathbf{d})$, where $\mathbf{d}$ is the displacement of the second unit cell from the first. This is a result of the Floquet condition [13] or Bloch's theorem [14], and is explained in more detail in Appendix A. As the wires are gold coated tungsten with a diameter of the order of micrometers, we model it with copper, which is intermediate in conductivity between the two. Using the nominal diameter of 20 μm, the calculation shown in Fig. 5 agrees with the measured result fairly well. If we increase the resistance as is done in Ref. [7], we may expect the transmission to decrease and the agreement to improve.

We now apply the cascading method to the left handed material studied in Sec. III A. We first repeat the calculation using the vector-electric potential method of Sec. II A, but for only one layer instead of all three layers in Fig. 1. This gives the Q matrices for one layer. Since all three layers are identical, we can then proceed to assemble them using the cascading method of Sec. II C. The physics issues are the
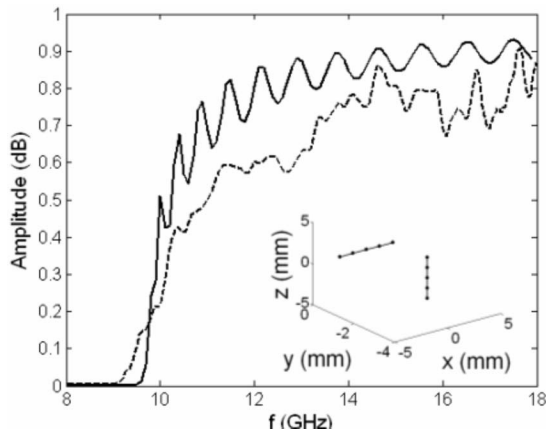
FIG. 5. The solid curves are the calculated transmission through 20 layers of the continuous wire structure whose unit cell is shown in the inset, where the dots mark the ends of the segments used. The dashed lines are the experimental results in [7].

same here. We model the elements with thin cylindrical wires running along the middle of the printed wires, assuming an equivalent radius of one-twelfth of the wire width. We approximate the substrate as a homogeneous medium by taking an average value of the permittivity of 1.12. The calculated results are shown in Fig. 6 and agree with the results in Fig. 2.

We now consider a thin wire element with the structure shown in Fig. 7(a). Four wires are joined at the origin. The other ends point towards four of the corners of a cube. These corners are at $(6\sqrt{2}, -6, 0)$, $(-6\sqrt{2}, -6, 0)$, $(0, 6, -6\sqrt{2})$, and $(0, 6, 6\sqrt{2})$, in millimeters. The length of each wire is 9 mm, and radius 0.1 mm. The basis vectors of the lattice are $\mathbf{a} = (12\sqrt{2}, 0, 0)$, $\mathbf{b} = (0, 0, 12\sqrt{2})$, and $\mathbf{c} = (6\sqrt{2}, 12, 6\sqrt{2})$ in mm. This can be shown to be an fcc lattice. We have chosen these to basis vectors to make it easy to apply the method. The presence of the junction requires an additional condition for the currents along the wires, which is that the charge densi-
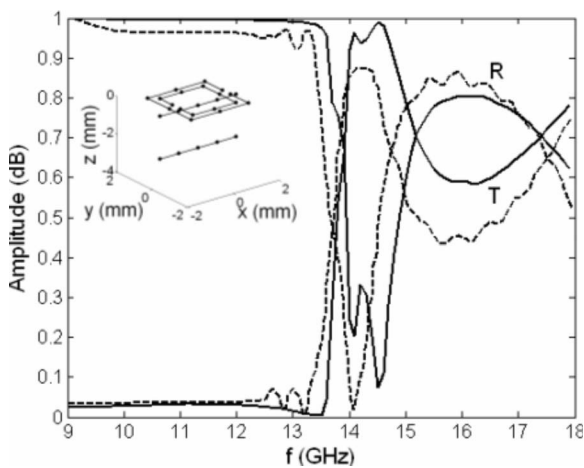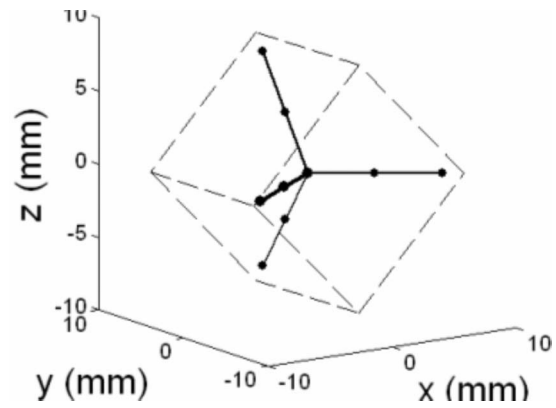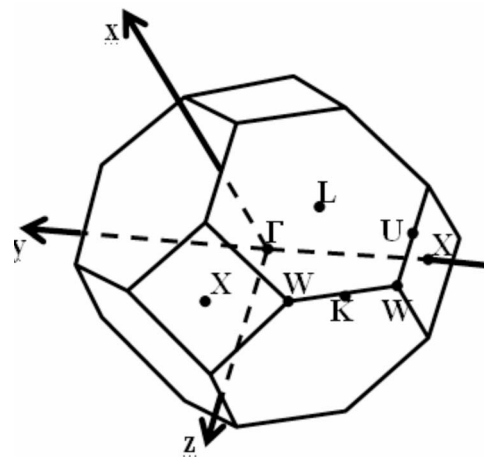

FIG. 6. The solid curves are the calculated transmission (T) through and reflection (R) from three layers of the left handed material whose unit cell is shown in the inset, where the dots mark the ends of the segments used. The dashed lines are the experimental results in [4].

(a)

(b)

FIG. 7. (a) The wire element in the photonic crystal. When repeated using the fcc basis vectors defined in the text, the edges of the cube shown just touch one another. (b) The Brillouin zone of the fcc lattice. Note the orientation of the axes for our definition of the basis vectors.

ties must be constant for all the wires in the neighborhood of the junction [12,25].

In order to map out the band structure, we consider the projection of the 3D polygon bounded by X, U, L, K, W [Fig. 7(b)] on to the xz plane. This forms a triangle. We compute the band structure with respect to k_y for each $\mathbf{K}_\parallel$ point along this triangle. These points are taken at intervals of 0.05, in units of c_y/π, where c_y is the y component of $\mathbf{c}$. Note that c_y/π is the distance of X from the origin. The frequency is taken from 0.2 to 20 GHz, at intervals of 0.2 GHz. For each frequency, the eigenvalue $\exp(-i\mathbf{k}\cdot\mathbf{c})$, in the Bloch wave equation is computed. This is divided by $\exp(-i\mathbf{K}_\parallel\cdot\mathbf{c})$ to give $\exp(-i\mathbf{k}_y c_y)$, and then solved for k_y. In principal, the magnitude of the eigenvalue should be 1 in order to give propagating Bloch waves. In practice, numerical errors and resistance losses mean that the calculated values would be slightly different from one. For our calculation, we have chosen to keep only magnitudes that are between 0.9 and 1.1. We can inter-
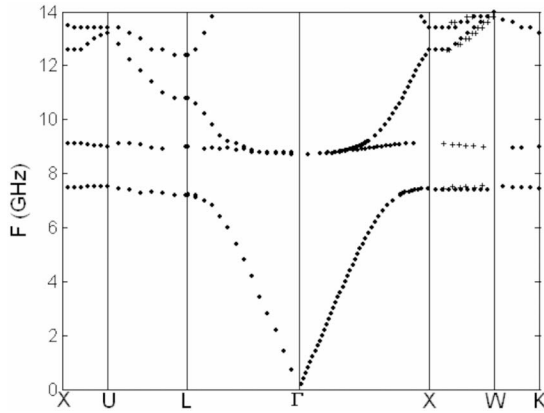
FIG. 8. Band structure for the fcc thin wire photonic crystal. The dots are obtained from interpolation in the k_y direction through points on *XULKW*. Γ is the projection of *X* on the *xz* plane, so the structure long ΓX is the k_y band at Γ. The crosses give the band structure along $X'W'$.

pret this physically. For a magnitude of $\exp(-i\mathbf{k}\cdot\mathbf{c})$ equal to 0.9, the intensity is attenuated by 0.9^2 after passing through one layer. This means it would decrease exponentially by about half after only three layers. 1.1 is approximately 1/0.9 and corresponds to decay in the opposite direction. If we use this to define the propagating distance, then our choice of the 0.9 and 1.1 range of eigenvalues keeps only Bloch waves that can propagate for more than three layers.

After computing the band structure in k_y for each point along the projection of *XULKW*, the band structure along the lines joining the actual symmetry points can then be mapped out. This is done for each $\mathbf{K}_\parallel$, by determining the k_y value of the corresponding point on *XULKW*, and then interpolating on the band structure to find all the propagating Bloch wave energies at that value of k_y. In this way, we obtain the band structure shown in Fig. 8. Notice the full band gap from 7.4 to 8.8 GHz. For our choice of α, this band gap should be interpreted as the energy range within which no wave can propagate for more than three layers. Conversely, it is also possible for waves outside the band gap to attenuate after three layers. We find that waves close to the band gap do tend to attenuate more than those further away.

X' and W' are equivalent symmetry points to X and W. From Fig. 7(b), X' happens to be the projection of W' on the *xz* plane. If $\mathbf{K}_\parallel$ is taken at X', the k_y band structure should be identical with the band structure along the *XW* line. We carry out the calculation and find that this is indeed the case, as shown by the crosses in Fig. 8. This serves as a confirmation of the accuracy of the method, as the two results are calculated along quite different $\mathbf{K}_\parallel$. From Fig. 7(b), the band structure along *XW* is calculated for **k** vectors close to normal incidence, whereas those along $X'W'$ are close to grazing angles. The band at 7.4 GHz has not appeared in the calculation along $X'W'$ because it is too narrow. It is possible to see this along *XW* because these are obtained by interpolating along band structures outside the *XW*.

This band gap is not wide compared to those reported of metallodielectric photonic crystals [5]. It is interesting nevertheless because the thin wires occupy such a small fraction of the volume. We have assumed that the medium has a permittivity of 1, which can be approximated by foam spacers, though the calculation could also be carried out for any homogeneous medium. We found that if we shorten the wires to 6 mm, keeping them connected at the junction, the upper band in Fig. 8 around Γ lowers and closes the gap. The same is true if we disconnect the wires at the junction. Examining the transmission and reflection through one layer of the photonic crystal shows a resonance that is similar to a periodic array of straight conducting fibers of length 18 mm, twice the length of each wire. It occurs at 8.3 GHz, exactly where the band gap is located, and close to where the lattice constant $|\mathbf{a}_3|$ is half a wavelength. This suggests that the complete gap arises as a result of strong increase in scattering at the Brillouin zone boundary. As the resonance frequency is directly related to the wire length, this offers a simple means of tuning the band gap.

IV. CONCLUSION

In conclusion, we have developed a method for calculating electromagnetic wave propagation through thin wire metamaterials, and demonstrated that a complete band gap is possible for a photonic crystal made up of only thin wires. This method combines phased array antenna calculation, FSS, design, and LEED theory, which we have shown to be reliable by comparison with experiments.

The method is developed specifically for metamaterials made up of thin wires only. Each element is therefore treated as a 1D object and discretized into segments. In FEM or FDTD methods, the thin wire would have to be treated as a 3D object. Even assuming that periodic condition and cascading are used throughout, a proper comparison among the methods is difficult as they involve different types of computation. Our method has relatively few unknowns per element, but requires summing of plane waves to convergence. In FEM, each segment would have to be further discretized into 3D elements. This would obviously increase the computational load significantly and perhaps unnecessarily. FDTD does not require a scan over frequencies, but would require sufficiently small discretization to model the element because it uses a rectangular grid. The closest of the existing methods is the well established PMM that is used for FSS design [13], and Fig. 4 shows that our method is faster by as much as two orders of magnitude.

We expect that our method can be used successfully when the wavelength is comparable to or longer than the wire segment, as is typical of the MoM method [12]. We also find by calculation that the appearance of a band gap despite the very low volume fraction of the elements is related to the thin wire resonance. We hope that an experiment can be carried out to verify this in the future.

ACKNOWLEDGMENTS

APPENDIX A

This choice of the basis function in Eq. (1) [12,21] appears to give three unknown coefficients per segment. In fact, it would reduce to one coefficient per segment when the conditions of continuity in current and charge density are imposed at the segment junctions. However, to obtain enough equations, one more condition on the current at each end of the wire is needed. Reference [12] gives an expression for the end cap current, relating the current gradient to the wire radius. Here we assume that the end cap current is negligible. This is valid for very thin wires as the end cap area is small.

Consider the E field of I_j at $\mathbf{R}_i$, the observation point on the surface at the center of the ith segment. This can be computed using the following equation [26]:

$$\mathbf{E} = -\nabla\phi - \frac{\partial \mathbf{A}}{\partial t}, \tag{A1}$$

where ϕ is the electric potential and $\mathbf{A}$ the vector potential, both due to I_j. In the time harmonic case, the component along the ith segment can be discretized as

$$E_{ij} = -\frac{\phi(\mathbf{R}_i + \delta l \mathbf{p}_i/2, \mathbf{R}_j) - \phi(\mathbf{R}_i - \delta l \mathbf{p}_i/2, \mathbf{R}_j)}{\delta l}$$
$$- i\omega \mathbf{A}(\mathbf{R}_i, \mathbf{R}_j) \cdot \mathbf{p}_i, \tag{A2}$$

where $\mathbf{p}_i$ is the unit vector parallel to segment i, and E_{ij} is the E-field component along segment i, due to I_j. δl is the distance over which the potential difference due to the charges on segment j is to be computed. In [17], δl is taken to be l_i, the full length of segment i. Since we are using the point matching method, δl should be a small fraction of this. We have used $0.01 l_i$ to $0.1 l_i$ for our simulation.

This approach separates the E field into a contribution from the charge density on segment j which produces ϕ, and a contribution for the current which gives $\mathbf{A}$. The charge density is obtained from the continuity equation [26]

$$\nabla \cdot \mathbf{J} + \frac{\partial \rho}{\partial t} = 0, \tag{A3}$$

where $\mathbf{J}$ is the current density and ρ the volume charge density. In the time harmonic case, this gives

$$\sigma_j = -\frac{1}{j\omega}\frac{dI_j}{ds}, \tag{A4}$$

where σ_j is the line charge density on segment j. Substituting Eq. (1) gives

$$\sigma_j = A_j \left[\frac{\delta(s - s_j + l_j/2)}{j\omega} - \frac{\delta(s - s_j - l_j/2)}{j\omega} \right]$$
$$\times B_j \left[-\beta l_j \frac{\cos\beta(s - s_i)}{j\omega l_j} + \sin\frac{\beta l_i}{2}\frac{\delta(s - s_j + l_j/2)}{j\omega} \right.$$
$$\left. + \sin\frac{\beta l_j}{2}\frac{\delta(s - s_j - l_j/2)}{j\omega} \right] + C_j \left[\beta l_j \frac{\sin\beta(s - s_j)}{j\omega l_j} \right.$$

$$\left. - \cos\frac{\beta l_j}{2}\frac{\delta(s - s_j + l_j/2)}{j\omega} + \cos\frac{\beta l_j}{2}\frac{\delta(s - s_j - l_j/2)}{j\omega} \right]. \tag{A5}$$

Note the appearance of δ functions. These appear because I_j terminates abruptly at the two ends of the isolated segment j. They correspond to point charges. The first two are the ones approximated as line charges in [17]. Fortunately, the requirement that the current be continuous at the junctions means that all point charges cancel exactly except for those at the two free ends of the wire element, where they can also be neglected because we have assumed that end cap currents are zero. Thus, the charge density reduces to

$$\sigma_j = -\frac{\beta B_j}{j\omega}\cos\beta(s - s_i) + \frac{\beta C_j}{j\omega}\sin\beta(s - s_j). \tag{A6}$$

The contribution of a length element dl on segment j to $\mathbf{A}$ and ϕ are then, following the notations of [13], given by [17]

$$d\mathbf{A} = \frac{Z I_j dl}{2j\omega D_x D_z}\hat{\mathbf{p}}_j \sum_{k=-\infty}^{\infty}\sum_{n=-\infty}^{\infty}\frac{\exp(-j\beta\mathbf{R}\cdot\hat{\mathbf{r}}_\pm)}{r_y}, \tag{A7}$$

and

$$d\phi = \frac{\sigma_j dl}{2j\varepsilon\beta D_x D_z}\sum_{k=-\infty}^{\infty}\sum_{n=-\infty}^{\infty}\frac{\exp(-j\beta\mathbf{R}\cdot\hat{\mathbf{r}}_\pm)}{r_y}, \tag{A8}$$

where D_x is the period along the x direction, D_z is the period along z, ε is the permittivity, and Z is the impedance $\sqrt{\mu/\varepsilon}$. $\mathbf{R}$ is the position vector of $\mathbf{R}_i$ relative to the element dl on segment j. Defining the original incident direction $\hat{\mathbf{s}}$ to be $\hat{\mathbf{x}}s_x + \hat{\mathbf{y}}s_y + \hat{\mathbf{z}}s_z$, $\hat{\mathbf{r}}_\pm$ is given by [13]

$$\hat{\mathbf{r}}_\pm = \hat{\mathbf{x}}\left(s_x + k\frac{\lambda}{D_x}\right) \pm \hat{\mathbf{y}}r_y + \hat{\mathbf{z}}\left(s_z + n\frac{\lambda}{D_z}\right), \tag{A9}$$

where

$$r_y = \sqrt{1 - \left(s_x + k\frac{\lambda}{D_x}\right)^2 - \left(s_z + n\frac{\lambda}{D_z}\right)^2}. \tag{A10}$$

The sign is to be chosen such that the plane wave sums in Eqs. (A7) and (A8) converge. This means the same sign as the y coordinate of $\mathbf{R}$. Note that the convention used for the square root sign for r_y is as follows: $\sqrt{x} = |\sqrt{x}|$ for $x \geq 0$, $\sqrt{x} = -j|\sqrt{-x}|$ for $x < 0$.

The unknown coefficients A_j, B_j, and C_j are then obtained by following a procedure similar to that used in the NEC MoM algorithm [12]. $d\mathbf{A}$ and $d\phi$ in Eqs. (A7) and (A8) can be manipulated in a very similar way to $d\mathbf{E}$, using the same techniques that are used in FSS calculations [13]—see Appendix B—to give E_{ij}. Point matching and Ohm's law then give

$$\left(E_i^{inc} + \sum_{j=1}^{N_s} E_{ij}\right)l_i = \bar{I}_i \bar{Z}_i, \tag{A11}$$

where E_i^{inc} is the tangential component of the incident E field at $\mathbf{R}_i$, so that the left hand side is approximately the total voltage across segment j. The averaged current, obtained by

averaging Eq. (1), is used on the right hand side,

$$\bar{I}_i = A_i + C_i \operatorname{sinc}(\beta l_i/2). \tag{A12}$$

The next set of equations is from continuity of current at segment junctions.

$$A_i + B_i \sin \frac{\beta l_i}{2} + C_i \cos \frac{\beta l_i}{2} = A_{i+1} - B_{i+1} \sin \frac{\beta l_{i+1}}{2}$$

$$+ C_{i+1} \cos \frac{\beta l_{i+1}}{2}. \tag{A13}$$

The third set is from continuity of line charge density.

$$B_i \cos \frac{\beta l_i}{2} - C_i \sin \frac{\beta l_i}{2} = B_{i+1} \cos \frac{\beta l_{i+1}}{2} + C_{i+1} \sin \frac{\beta l_{i+1}}{2}. \tag{A14}$$

The last set is from assumption of zero end cap current.

$$A_1 - B_1 \sin \frac{\beta l_1}{2} + C_1 \cos \frac{\beta l_1}{2} = A_{N_s} + B_{N_s} \sin \frac{\beta l_{N_s}}{2}$$

$$+ C_{N_s} \cos \frac{\beta l_{N_s}}{2} = 0. \tag{A15}$$

These four sets of equations form a linear system which can be solved using Gaussian elimination.

In a continuous wire structure, it is possible for wires to continue from one unit cell into an adjacent unit cell. Figure 1, for example, shows three unit cells in which each cell consists of two wires that are continuous into adjacent cells. In such cases, additional equations are needed to ensure the smoothness of current across the unit cell wall. Consider two segments i and j. Suppose that segment i on the adjacent unit cell is connected to segment j in the original cell through the common cell wall. Suppose that this adjacent unit cell is displaced from the original unit cell by a vector $\mathbf{d}$. Using the Floquet condition [13], the current on segment i in the adjacent cell should differ from the current on segment i in the original cell by a factor of $\exp(-j\beta\hat{\mathbf{s}}\cdot\mathbf{d})$. Suppose further that the end of segment j meets the start of segment i of the adjacent cell. Then Eqs. (A13) and (A14) must be rewritten for these two segments as

$$A_j + B_j \sin \frac{\beta l_j}{2} + C_j \cos \frac{\beta l_j}{2}$$

$$= \exp(-j\beta\hat{\mathbf{s}}\cdot\mathbf{d})\left(A_i - B_i \sin \frac{\beta l_i}{2} + C_i \cos \frac{\beta l_i}{2}\right), \tag{A16}$$

and

$$B_j \cos \frac{\beta l_j}{2} - C_j \sin \frac{\beta l_j}{2}$$

$$= \exp(-j\beta\hat{\mathbf{s}}\cdot\mathbf{d})\left(B_i \cos \frac{\beta l_i}{2} + C_i \sin \frac{\beta l_i}{2}\right). \tag{A17}$$

For the case in Fig. 1, for instance, $\mathbf{d} = \hat{\mathbf{x}}D_x$.

APPENDIX B

The derivation of the vector-electric potential method from first principles has been described in [17,18]. We provide here an alternative derivation from the direct E-field method to show the close connection between the two. We also offer an explanation for the much faster convergence of the vector-electric potential method.

The E-field contribution from an infinitesimal wire length dl is given by [13]

$$d\mathbf{E} = I_{00}dl \frac{Z}{2D_xD_z} \sum_{k=-\infty}^{\infty} \sum_{n=-\infty}^{\infty} \frac{\exp(-j\beta\mathbf{R}\cdot\hat{\mathbf{r}}_\pm)}{r_y}\bar{\mathbf{e}}_\pm, \tag{B1}$$

where $\bar{\mathbf{e}}_\pm = (\hat{\mathbf{p}}_j \times \hat{\mathbf{r}}_\pm) \times \hat{\mathbf{r}}_\pm$. $\mathbf{R}$ here is the position of the observation point relative to dl. As we are dealing with typical FSS, we shall only consider wire elements lying in the plane of the array. We choose the observation point such that its y coordinate relative to the array plane is $+a$, where a is the wire radius. Then the $+$ sign in the above expression has to be chosen so that convergence is possible. For a general current distribution $I(l)$ over segment j of the wire element, such as the one in Eq. (1), the E field from the whole segment is obtained by integrating Eq. (B1) as follows:

$$\mathbf{E} = \frac{Z}{2D_xD_z} \sum_{k=-\infty}^{\infty} \sum_{n=-\infty}^{\infty} \bar{\mathbf{e}}_+ \int_{-l_j/2}^{l_j/2} \frac{\exp(-j\beta\mathbf{R}\cdot\hat{\mathbf{r}}_+)}{r_y} I(l)dl = \frac{Z}{2D_xD_z} \sum_{k=-\infty}^{\infty} \sum_{n=-\infty}^{\infty} \frac{\exp[-j\beta(\mathbf{R}-\mathbf{R}_j)\cdot\mathbf{r}_+]}{r_y}\bar{\mathbf{e}}_+ \int_{-l_j/2}^{l_j/2} \frac{\exp(-j\beta l\hat{\mathbf{p}}_j \cdot \mathbf{r}_+)}{r_y} I(l)dl. \tag{B2}$$

From Ref. [13], $\bar{\mathbf{e}}_\pm = (\hat{\mathbf{p}}\cdot\hat{\mathbf{r}}_\pm)\hat{\mathbf{r}}_\pm - \hat{\mathbf{p}}$, so that

$$\mathbf{E} = \frac{Z}{2D_xD_z} \sum_{k=-\infty}^{\infty} \sum_{n=-\infty}^{\infty} \frac{\exp[-j\beta(\mathbf{R}-\mathbf{R}_j)\cdot\hat{\mathbf{r}}_+]}{r_y}(\hat{\mathbf{p}}_j\cdot\hat{\mathbf{r}}_+)\hat{\mathbf{r}}_+ \int_{-l_j/2}^{l_j/2} I(l)\exp(-j\beta l\hat{\mathbf{p}}_j \cdot \hat{\mathbf{r}}_+)dl - \frac{\exp[-j\beta(\mathbf{R}-\mathbf{R}_1)\cdot\hat{\mathbf{r}}_+]}{r_y}\hat{\mathbf{p}}_j$$

$$\times \int_{-l_j/2}^{l_j/2} I(l)\exp(-j\beta l\hat{\mathbf{p}}_j\cdot\hat{\mathbf{r}}_+)^d l. \tag{B3}$$

Integrating the first term by parts,

$$\mathbf{E} = \frac{Z}{2D_xD_z} \sum_{k=-\infty}^{\infty} \sum_{n=-\infty}^{\infty} - \frac{\exp[-j\beta(\mathbf{R}-\mathbf{R}_1)\cdot\hat{\mathbf{r}}_+]}{r_y} \hat{\mathbf{p}}_j \int_{-l_j/2}^{l_j/2} I(l)\exp(-j\beta l\hat{\mathbf{p}}_j\cdot\hat{\mathbf{r}}_+)dl$$

$$+ \frac{\exp[-j\beta(\mathbf{R}-\mathbf{R}_j)\cdot\hat{\mathbf{r}}_+]}{r_y}\left\{\left[I(l)\frac{\exp(-j\beta l\hat{\mathbf{p}}_j\cdot\hat{\mathbf{r}}_+)}{(-j\beta\hat{\mathbf{p}}_j\cdot\hat{\mathbf{r}}_+)}\right]_{-l_j/2}^{l_j/2} - \int_{-l_j/2}^{l_j/2}\frac{dI}{dl}\frac{\exp(-j\beta l\hat{\mathbf{p}}_j\cdot\hat{\mathbf{r}}_+)}{(-j\beta\hat{\mathbf{p}}_j\cdot\hat{\mathbf{r}}_+)}dl\right\}(\hat{\mathbf{p}}_j\cdot\hat{\mathbf{r}}_+)\hat{\mathbf{r}}_+. \tag{B4}$$

From the formula for the line charge density in Eqs. (A4) and (5),

$$\mathbf{E} = \frac{Z}{2D_xD_z} \sum_{k=-\infty}^{\infty} \sum_{n=-\infty}^{\infty} - \frac{\exp[-j\beta(\mathbf{R}-\mathbf{R}_1)\cdot\hat{\mathbf{r}}_+]}{r_y} \hat{\mathbf{p}}_j \int_{-l_j/2}^{l_j/2} I(l)\exp(-j\beta l\hat{\mathbf{p}}_j\cdot\hat{\mathbf{r}}_+)dl$$

$$+ \frac{\exp[-j\beta(\mathbf{R}-\mathbf{R}_j)\cdot\hat{\mathbf{r}}_+]}{r_y}\left\{\left[I(l)\frac{\exp(-j\beta l\hat{\mathbf{p}}_j\cdot\hat{\mathbf{r}}_+)}{(-j\beta\hat{\mathbf{p}}_j\cdot\hat{\mathbf{r}}_+)}\right]_{-l_j/2}^{l_j/2} - \int_{-l_j/2}^{l_j/2}j\omega\sigma(l)\frac{\exp(-j\beta l\hat{\mathbf{p}}_j\cdot\hat{\mathbf{r}}_+)}{(-j\beta\hat{\mathbf{p}}_j\cdot\hat{\mathbf{r}}_+)}dl\right\}(\hat{\mathbf{p}}_j\cdot\hat{\mathbf{r}}_+)\hat{\mathbf{r}}_+$$

$$= \frac{Z}{2D_xD_z} \sum_{k=-\infty}^{\infty} \sum_{n=-\infty}^{\infty} - \frac{\exp[-j\beta(\mathbf{R}-\mathbf{R}_j)\cdot\hat{\mathbf{r}}_+]}{r_y}\left\{\hat{\mathbf{p}}_j\int_{-l_j/2}^{l_j/2} I(l)\exp(-j\beta l\hat{\mathbf{p}}_j\cdot\hat{\mathbf{r}}_+)dl\right\} - \frac{\omega\exp[-j\beta(\mathbf{R}-\mathbf{R}_j)\cdot\hat{\mathbf{r}}_+]}{\beta r_y}\hat{\mathbf{r}}_+\int_{-l_j/2}^{l_j/2}\sigma(l)$$

$$\times\exp(-j\beta l\hat{\mathbf{p}}_j\cdot\hat{\mathbf{r}}_+)dl + I(l_j/2)\hat{\mathbf{r}}_+\frac{\exp[-j\beta(\mathbf{R}-\mathbf{R}_a)\cdot\hat{\mathbf{r}}_+]}{j\beta r_y} - I(-l_j/2)\hat{\mathbf{r}}_+\frac{\exp[-j\beta(\mathbf{R}-\mathbf{R}_b)\cdot\hat{\mathbf{r}}_+]}{j\beta r_y}. \tag{B5}$$

where $\mathbf{R}_a$ is the end of segment j, and $\mathbf{R}_b$ is the start.

These terms can now be interpreted physically. The first term comes from the vector potential. The second term is the contribution from the charge distribution over segment j. The third term is the E field from a point charge at the start of the segment. The fourth term is the E field from a point charge at the start of the segment. To see that this is indeed the case, we compare this with the plane wave expansions for the vector potential and electric potential given in Eqs. (A7) and (A8) for an infinitesimal wire length. Comparing the first term in Eq. (B5) with the expansion for $d\mathbf{A}$, we see that the first term is in fact $-j\omega\mathbf{A}$, where $\mathbf{A}$ is obtained from $d\mathbf{A}$ by integrating over segment j. To compare the remaining terms, we must first derive the E-field from $d\phi$. This is obtained by taking its negative gradient with respect to $\mathbf{R}$,

$$d\mathbf{E} = -\nabla(d\phi) = -\frac{\sigma_j dl}{2\varepsilon D_xD_z}\hat{\mathbf{r}}_\pm \sum_{k=-\infty}^{\infty} \sum_{n=-\infty}^{\infty} \frac{\exp(-j\beta\mathbf{R}\cdot\hat{\mathbf{r}}_\pm)}{r_y}. \tag{B6}$$

This can be interpreted as the E field of a point charge of magnitude σdl. Notice that it is different from $d\mathbf{E}$ of Eq. (B1), because the latter has contributions from the current on dl as well as two charges at the start and end points. Comparing this E field for a point charge with the second to fourth terms in Eq. (B5), we see from the common presence of $\hat{\mathbf{r}}$ that these latter terms may indeed come from charges. A more detailed comparison would show that the second term in Eq. (B5) comes from integrating Eq. (B6) over segment j for a line charge of distribution $\sigma(l)$. Likewise, the third term comes from a point charge of charge $-I(l_j/2)$ at the end of segment j, and the fourth term comes from a point charge of charge $+I(-l_j/2)$ at the start of segment j. We have thus shown that Eq. (B5) is in fact the time harmonic form of

$$\mathbf{E} = -\nabla\phi - \frac{\partial\mathbf{A}}{\partial t}, \tag{B7}$$

from which the vector-electric potential is derived in [17,18].

As explained in [18], the requirement for continuity in current at junctions of segments means that point charges at segment junctions cancel exactly. The assumption of zero end cap currents means that point charges at the free ends of the wire element have zero magnitudes. Thus, the point charges in Eq. (B5), represented by the third and fourth terms, can be omitted, giving

$$\mathbf{E} = \frac{Z}{2D_xD_z} \sum_{k=-\infty}^{\infty} \sum_{n=-\infty}^{\infty} - \frac{\exp[-j\beta(\mathbf{R}-\mathbf{R}_j)\cdot\hat{\mathbf{r}}_+]}{r_y}\hat{\mathbf{p}}_j \int_{-l_j/2}^{l_j/2} I(l)$$

$$\times\exp(-j\beta l\hat{\mathbf{p}}_j\cdot\hat{\mathbf{r}}_+)dl$$

$$- \frac{\omega\exp[-j\beta(\mathbf{R}-\mathbf{R}_j)\cdot\hat{\mathbf{r}}_+]}{\beta r_y}\hat{\mathbf{r}}_+\int_{-l_j/2}^{l_j/2}\sigma(l)$$

$$\times\exp(-j\beta l\hat{\mathbf{p}}_j\cdot\hat{\mathbf{r}}_+)dl$$

$$= -j\omega\mathbf{A}(\mathbf{R},\mathbf{R}_j) - \nabla\phi(\mathbf{R},\mathbf{R}_j). \tag{B8}$$

Note that this is not the actual E field due to the array of isolated segment j, but will give the actual E field of the array of the whole wire element when summed over all segments using a current that satisfies the properties just mentioned. In the second term, the components of $\hat{\mathbf{r}}_+$ increase in magnitude as k and n increase during the summation over them. Recall from Eq. (B6) that $\hat{\mathbf{r}}_+$ comes from taking the gradient of the electric potential in Eq. (A8), which does not contain $\hat{\mathbf{r}}_+$ and should therefore be able to converge faster. With $\mathbf{A}$ and ϕ defined as in Eq. (B8), we can also calculate the E field along the observation segment i by discretizing the potential instead of using Eq. (B8) directly as follows:

$$\mathbf{E} \cdot \hat{\mathbf{p}}_i = - j\omega \mathbf{A}(\mathbf{R}_i, \mathbf{R}_j) \cdot \hat{\mathbf{p}}_i$$
$$- \frac{\phi(\mathbf{R}_i + \delta l \hat{\mathbf{p}}_i/2, \mathbf{R}_j) - \phi(\mathbf{R}_i - \delta l \hat{\mathbf{p}}_i/2, \mathbf{R}_j)}{\delta l}. \quad (B9)$$

This is the expression used in our implementation of the vector-electric potential method, originally motivated by a similar treatment in [17].

As we have shown in Fig. 3, where δl is chosen to be $0.01l_j$, this works well. Not only does it give comparable accuracy with the direct E-field method, but it converges much faster. In order to see the reason for this, we compare the plane wave summation for the two methods for the case when $I(l) = 1$ on segment j. For the direct E-field method, evaluation of Eq. (B2) gives

$$\mathbf{E} = \frac{Z}{2D_x D_z} \sum_{k=-\infty}^{\infty} \sum_{n=-\infty}^{\infty} \frac{\exp[-j\beta(\mathbf{R}_i - \mathbf{R}_j) \cdot \hat{\mathbf{r}}_\pm]}{r_y}$$
$$\times \mathrm{sinc}(\beta \mathbf{p}_j \cdot \hat{\mathbf{r}}_\pm l_j/2) \overline{\mathbf{e}}_\pm. \quad (B10)$$

For the vector-electric potential method, the required summations are obtained by integrating Eqs. (A7) and (A8) as follows:

$$\mathbf{A} = \frac{\eta}{2j\omega D_x D_z} \mathbf{p}_j \sum_{k=-\infty}^{\infty} \sum_{n=-\infty}^{\infty} \frac{\exp[-j\beta(\mathbf{R}_i - \mathbf{R}_j) \cdot \hat{\mathbf{r}}_\pm]}{r_y}$$
$$\times \mathrm{sinc}(\beta \hat{\mathbf{p}}_j \cdot \hat{\mathbf{r}}_\pm l_j/2), \quad (B11)$$

$$\phi = \frac{1}{2jk\varepsilon D_x D_z} \sum_{k=-\infty}^{\infty} \sum_{n=-\infty}^{\infty} \frac{\exp[-j\beta(\mathbf{R}_i - \mathbf{R}_j) \cdot \hat{\mathbf{r}}_\pm]}{r_y}$$
$$\times \mathrm{sinc}(\beta \hat{\mathbf{p}}_j \cdot \hat{\mathbf{r}}_\pm l_j/2), \quad (B12)$$

which would then be used in Eq. (B9). Note that the summations for both $\mathbf{A}$ and ϕ have essentially the same form. In all cases, the increasing quantities are the components of $\hat{\mathbf{r}}_+$. Extracting only the parts in Eq. (B10) containing these components gives terms of the form

$$\sum_{k=-\infty}^{\infty} \sum_{n=-\infty}^{\infty} \frac{\exp(-j\beta\mathbf{R} \cdot \hat{\mathbf{r}}_\pm)}{r_y(\beta\hat{\mathbf{p}}_j \cdot \hat{\mathbf{r}}_\pm l_j/2)} [(\hat{\mathbf{p}} \times \hat{\mathbf{r}}_\pm) \times \hat{\mathbf{r}}_\pm]$$
$$\to \int_1^\infty \frac{\exp(-\beta y r)}{r^2} r^2 2\pi r dr. \quad (B13)$$

Extracting the corresponding parts in Eqs. (B11) and (B12) gives terms of the form

$$\sum_{k=-\infty}^{\infty} \sum_{n=-\infty}^{\infty} \frac{\exp(-j\beta\mathbf{R} \cdot \hat{\mathbf{r}}_\pm)}{r_y(\beta\hat{\mathbf{p}}_j \cdot \hat{\mathbf{r}}_\pm l_j/2)} \to \int_1^\infty \frac{\exp(-\beta y r)}{r^2} 2\pi r dr. \quad (B14)$$

The integrals on the right hand side show the order of magnitude of the sums for large values of (k, n), when $r = \sqrt{r_x^2 + r_z^2}$ also become large. (Note that r here is not the actual magnitude of $\hat{\mathbf{r}}_+$, which is 1.) We have set the lower limit of the integrals to 1 to avoid the singularity that can occur if r is zero. This does not affect the reasoning as we only compare the rate of convergence for large r. The value of y is the radius of the wire, which is also the displacement of the observation point from the array plane of the axis of segment j. In both integrals, the factor of $\exp(-\beta y r)$ would force them to converge. However, the first integral would converge more slowly because of the increasing factor of r, whereas the second integral would converge more rapidly because it has a decreasing factor of $1/r$. This difference by a factor of r^2 explains why the vector-electric potential method can be faster than the direct E-field method by one to two orders of magnitude as shown in Fig. 4, despite the fact that more than one summation is required by Eq. (B9) for the former method. Note also that if y becomes zero, the first integral diverges because the integrand oscillates with increasing amplitude. However, the second integral can still converge because the integrand oscillates with decreasing amplitude. This can explain the trends in Fig. 4 which show that as the wire radius decreases, the computation time for the vector-electric potential method seems to approach a fixed value, whereas the time for the direct E-field method continues to increase in a straight line. The property that the sum converges even when the observation point lies in the array plane is also the reason why the vector-electric potential method is suitable for tilted elements in [17,18].

[1] P. Lodahl *et al.*, Nature (London) **430**, 654 (2004).
[2] P. Vukusic and J. R. Sambles, Nature (London) **424**, 852 (2003).
[3] E. I. Smirnova, I. Mastovsky, M. A. Shapiro, R. J. Temkin, L. M. Earley, and R. L. Edwards, Phys. Rev. ST Accel. Beams **8**, 091302 (2005).
[4] K. Li *et al.*, Appl. Phys. Lett. **82**, 2535 (2003).
[5] D. F. Sievenpiper, E. Yablonovitch, J. N. Winn, S. Fan, P. R. Villeneuve, and J. D. Joanrio poulos, Phys. Rev. Lett. **80**, 2829 (1998).
[6] E. Yablonovitch, T. J. Gmitter, and K. M. Leung, Phys. Rev. Lett. **67**, 2295 (1991).
[7] J. B. Pendry *et al.*, J. Phys.: Condens. Matter **10**, 4785 (1998).
[8] D. F. Sievenpiper, M. E. Sickmiller, and E. Yablonovitch, Phys. Rev. Lett. **76**, 2480 (1996).
[9] O. Einarsson, *Electromagnetic and Acoustic Scattering by Simple Shapes*, edited by J. J. Bowman, T. B. A. Senior, and P. L. E. Uslenghi (Hemisphere Publishing, New York, 1987), pp. 472–502.
[10] P. Markos and C. M. Soukoulis, Phys. Rev. E **65**, 036622 (2002).
[11] A. F. Peterson, S. L. Ray, and R. Mittra, *Computational Methods for Electromagnetics* (Oxford University Press, New York, 1997).

[12] J. Burke and A. Poggio, *Part I: NEC Program Description—Theory*, pp. 11and *Part I: NEC Program Description–Theory*, 12; *Part III: NEC User's Guide, Numerical Electromagnetics Code (NEC)—Method of Moments*, UCID 18834 (Lawrence Livermore Laboratory, California, 1981), p. 9; http://www.nec2.org

[13] B. A. Munk, *Frequency Selective Surfaces* (John Wiley & Sons, New York, 2000), pp. 79–107, *Frequency Selective Surfaces* (John Wiley & Sons, New York, 2000), pp. 125–142, *Frequency Selective Surfaces* (John Wiley & Sons, New York, 2000), pp. 381–383.

[14] J. B. Pendry, *Low Energy Electron Diffraction* (Academic Press, London, 1974), pp. 84,96,123,138.

[15] J. B. Pendry, J. Mod. Opt. **41**, 209 (1994).

[16] T. K. Wu, *Frequency Selective Surface and Grid Array* (Wiley, New York, 1995), Chap. 3, pp. 87–111.

[17] H. K. Schuman, D. R. Pflug, and L. D. Thompson, IEEE Trans. Antennas Propag. **32**, 364 (1984).

[18] K. M. Hock, IEEE Trans. Microwave Theory Tech. **54**, 648 (2006).

[19] P. Markos and C. M. Soukoulis, Phys. Rev. E **65**, 036622 (2002).

[20] J.-F. Ma, R. Mittra, and N. T. Huang, IEEE Trans. Antennas Propag. **53**, 1401 (2005).

[21] Y. S. Yeh and K. K. Mei, IEEE Trans. Antennas Propag. **AP-15**, 634 (1967).

[22] S. Ramo, J. R. Whinnery, and T. Van Duzer, *Fields and Waves in Communication Electronics*, 3rd ed. (Wiley, New York, 1994), pp. 180–185.

[23] C. G. Parazzoli, R. B. Greegor, K. Li, B. E. C. Koltenbah, and M. Tanielian, Phys. Rev. Lett. **90**, 107401 (2003).

[24] K. M. Hock and P.-M. Jacquart *et al.*, in *Electromagnetic Materials*, Proceedings of the Symposium R, Third International Conference on Materials for Advanced Technologies, ICMAT 2005, Singapore, 2005, (World Scientific, Singapore, 2005), pp. 200–203.

[25] R. W. Burton and R. W. P. King, IEEE Trans. Antennas Propag. **AP-23**, 657 (1975).

[26] J. D. Jackson, *Classical Electrodynamics* (John Wiley & Sons, New York, 1999), pp. 3 and *Classical Electrodynamics* (John Wiley & Sons, New York, 1999), 239.